Four-Dimensional Electron Microscopy

Ahmed H. Zewail, *et al.*

Science **328**, 187 (2010);
DOI: 10.1126/science.1166135

Four-Dimensional Electron Microscopy

Ahmed H. Zewail

The discovery of the electron over a century ago and the realization of its dual character have given birth to one of the two most powerful imaging instruments: the electron microscope. The electron microscope's ability to resolve three-dimensional (3D) structures on the atomic scale is continuing to affect different fields, including materials science and biology. In this Review, we highlight recent developments and inventions made by introducing the fourth dimension of time in electron microscopy. Today, ultrafast electron microscopy (4D UEM) enables a resolution that is 10 orders of magnitude better than that of conventional microscopes, which are limited by the video-camera rate of recording. After presenting the central concept involved, that of single-electron stroboscopic imaging, we discuss prototypical applications, which include the visualization of complex structures when unfolding on different length and time scales. The developed UEM variant techniques are several, and here we illucidate convergent-beam and near-field imaging, as well as tomography and scanning-pulse microscopy. We conclude with current explorations in imaging of nanomaterials and biostructures and an outlook on possible future directions in space-time, 4D electron microscopy.

The microscope and the telescope are arguably among the most powerful human-made instruments. To our vision, they have brought the very small and the very far away. Robert Hooke, for his *Micrographia*, chose the subtitle *Some Physiological Descriptions of Minute Bodies Made by Magnifying Glasses with Observations and Inquiries Thereupon* (*1*). These words were made in reference to the traditional optical microscope, for which the spatial resolution is limited by the wavelength of light; centuries later, major advances by new variant techniques have resulted in the crossing of such a limit (*2*–*4*). The transmission electron microscope (TEM), since its invention in the 1930s (*5*), has provided wavelengths on the picometer scale, taking the field of imaging beyond the "minutes" of Hooke's 17th-century *Micrographia*: It has become possible to image atoms in real space, reaching resolutions below 0.1 nm. The scope of applications (*6*) spans essentially all of the physical sciences and includes biology. Until recently, the structures determined in these studies were time-averaged over seconds of recording.

To reach the ultrashort time resolution of atomic motions (*7*), and at the same time maintain the high spatial resolution, a different approach from that of the millisecond-limited TEM or the nanosecond high-speed imaging method had to be conceived. In conventional microscopes, the electrons are produced by heating the source or by field emission, resulting in randomly distributed bursts of a continuous electron beam. Photoelectron emission from a cathode can provide ultrashort pulses of electrons for time-resolved diffraction, as discussed below and detailed elsewhere (*8*); but for imaging, the use of a large number of electrons in a pulse imposes limits on the temporal and spatial resolutions of the microscope. This is because repulsion between electrons prevents the attainment of high spatiotemporal resolutions, and it is not feasible to image the ultrafast elementary dynamics of a complex transformation. The challenge was then in obtaining the high spatial resolution of conventional electron microscopy (EM) but simultaneously enabling the temporal resolution of atomic-scale motions.

In this Review, we discuss the development of four-dimensional ultrafast electron microscopy (4D UEM) (*9*–*11*) and summarize applications (*12*) that illustrate the potential of the approach. In UEM space-time domains (Fig. 1), images are obtained stroboscopically with single-electron coherent packets. Under such a condition, electron repulsion is absent, permitting real-space imaging, Fourier-space diffraction, and energy-space electron spectroscopy with high spatiotemporal resolutions. The time resolution becomes limited only by the laser pulse width and energy width of the packets, the camera rate of recording becomes irrelevant for the temporal resolution, and the delay between pulses can be controlled to allow for the cooling of the specimen and/or repetitiveness of the specimen's exposure. The applications given here are selected to display phenomena of different length and time scales, from atomic motions in structural dynamics, to phase transitions, to membrane mechanical drumming. We also discuss single-pulse and single-particle imaging, using convergent-beam UEM, and include the recent developments of techniques for nanomaterials and biological structures. To begin, it is instructive to discuss the concepts involved in 4D microscopy imaging.

Single-Electron Imaging: Space and Time

Since its original use in viewing rotating objects, a stroboscope (*strobos* from the Greek word for "whirling" and *scope* from the Greek for "look at") can produce, with appropriately chosen pulses of light, a well-resolved image of a moving object, such as a bullet or a falling apple. Thus, the pulse duration plays the same role as the opening of a camera shutter. The time duration required to observe, with high definition, transformations in which atoms move at speeds of the order of 1 km/s is in the femtosecond domain, and although laser light pulses can capture atoms in motion (*7*), they cannot, for complex structures, image the positions of all atoms in space because of the limitation imposed by their relatively long wavelength. Accelerated electrons, however, waive such a restriction.

The concept of single-electron imaging is based on the premise that trajectories of coherent and timed single-electron packets can provide an image that is equivalent to that obtained by using many electrons in conventional microscopes. Unlike the random electron distribution of con-

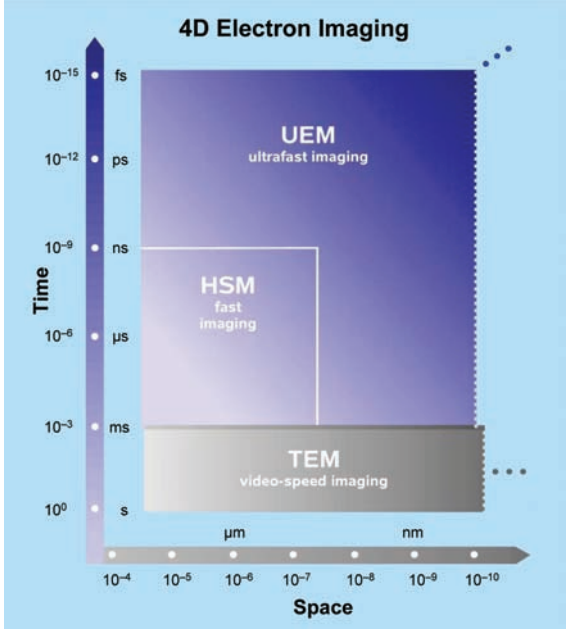

Fig. 1. 4D electron imaging. The resolution boundaries of ultrafast imaging are compared with those achieved in conventional TEM, limited by the speed of video camera, and, in high-speed microscopy (HSM), defined by the rectangle shown. The spatiotemporal scales of UEM achieved to date are outlined with possible future extensions. The approaches of single-electron and single-pulse imaging are fundamentally different because of the limiting problem of space-charge described in the text.

Physical Biology Center for Ultrafast Science & Technology, California Institute of Technology, Pasadena, CA 91125, USA. E-mail: zewail@caltech.edu

ventional microscopes, in UEM, the packets are timed with femtosecond precision, and each electron has a unique coherence volume (Fig. 2). Each electron with de Broglie's "pilot waves" (*13*) is (transversely) coherent over the object length scale to be imaged, with a longitudinal coherence length that depends on the electron's velocity; on the detector, the electron produces a "click," behaving as a classical particle. When a sufficient number of such clicks is accumulated stroboscopically, the whole image emerges. In other words, "each electron interferes only with itself." In the microscope, the electron pulse that produces the image is termed the probe pulse, and in ultrafast imaging with a train of such pulses, the number of frames in a movie could be higher than 10^{12} per second; as such, this stop-motion photography constitutes a real-time movie of the process.

To visualize the motion, the molecule or material must be launched on its path by using a femtosecond initiation optical pulse, called the clocking or pump pulse, thus establishing a temporal reference point (time zero) for the changes that occur in the motion. By sending the clocking pulse along an adjustable optical path, we can precisely fix each probe frame on the time axis: Knowing the speed of light, a typical optical path accuracy of 1 μm corresponds to absolute timing of the snapshots of 3.3 fs. Because the clocking pulse is controlled to precede each electron pulse, the time axis is defined by the separation between them and is no longer limited by the response of the video detector in the microscope. Lastly, to synchronize the motion of many independent atoms or molecules so that all of them have reached a similar point in the course of their structural evolution, the relative timing of clocking and probe pulses must be of femtosecond precision, and the launch configuration must be defined to sub-angstrom resolution.

In imaging with electrons (fermions), unlike with photons (bosons), we must also consider consequences of the Pauli exclusion principle. The maximum number of electrons that can be packed into a state (or a cell of phase space) is two, one for each spin; in contrast, billions of photons can be condensed in a state of the laser radiation. This characteristic of electrons represents a fundamental difference in what is termed the "degeneracy," or the mean number of electrons per cell in phase space. Typically it is about 10^{-4} to 10^{-6}, but it is possible in UEM to increase the degeneracy by orders of magnitude, a feature that could be exploited for studies in quantum electron optics (*12*). We note here that the definition of a "single electron packet" is reserved for the case when each timed packet contains one, or a small number, of electrons such that the Coulombic repulsion is effectively absent.

The temporal (longitudinal) coherence length of the packet is simply given by $l_{tc} = v_e \cdot (h/\Delta E)$, with the width ΔE being determined by the energy of the photoelectrons relative to the work function of the cathode, v_e is the electron velocity,

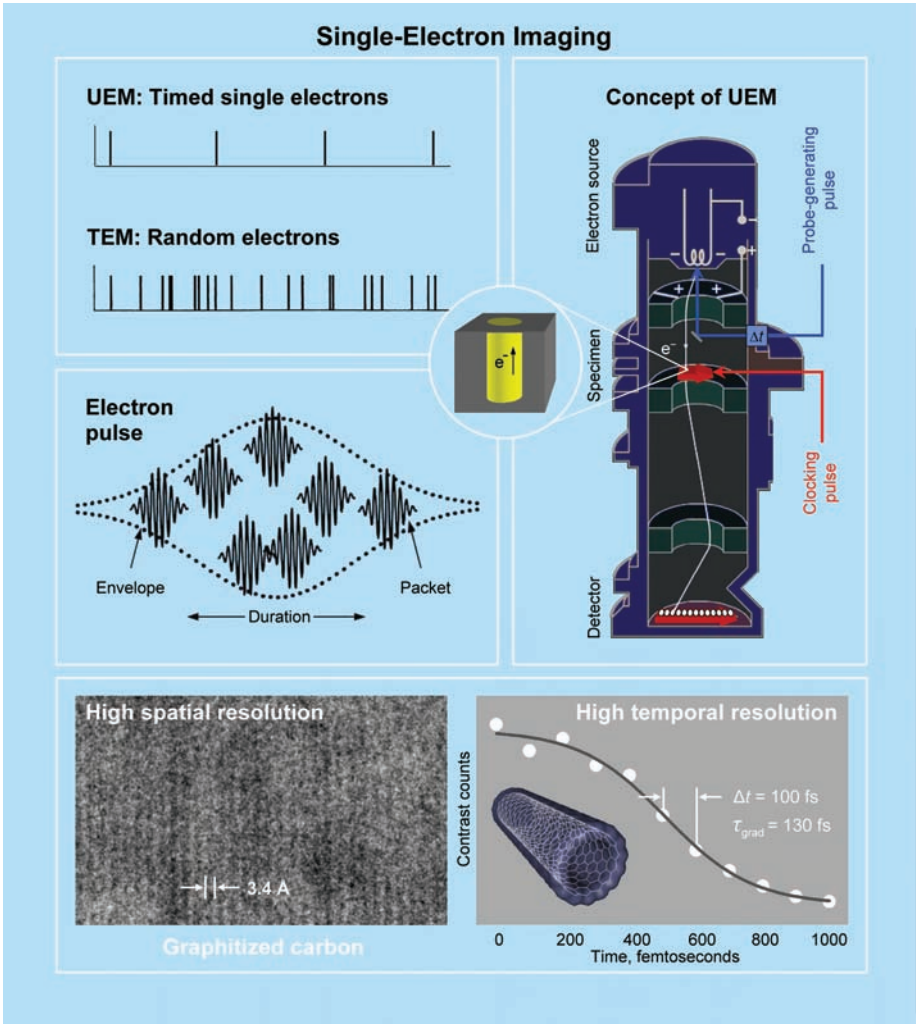

Fig. 2. Conceptual and experimental realization of single-electron imaging. Shown are schematics of timed single-electron packets (UEM) and random electrons (conventional TEM) used in imaging (upper left). Also depicted is the electron-pulse envelope together with individual electron packets (center left). A single-electron trajectory is schematized in the microscope together with an illustration of what is meant by a coherence volume (upper right; see text). The bottom panel displays a high-resolution UEM image of graphitized carbon with lattice-plane separations of 3.4 Å (left), and a temporal profile obtained from the images of evanescent fields in carbon nanotubes; the time steps are of 100-fs duration, and the rate of change is given by the gradient (τ_{grad} = 130 fs), which is determined by the materials response and pulse widths involved (see the section on near-field UEM and Fig. 5). The experimental data are from (*10*, *46*).

and h is Planck's constant. The spatial (transverse) coherence length (l_{sc}) is a measure of the beam coherence and is given by $h/\Delta P_T$, where ΔP_T is the transverse momentum spread; it can be expressed in terms of the source angular deviation (α) at the specimen, $l_{sc} = \lambda_e/\alpha$, by simply dividing both the numerator and denominator of $h/\Delta P_T$ by the longitudinal momentum value. The coherence volume of each cell becomes

$$V_c(\text{cell}) \equiv \Delta x \Delta y \Delta z = l_{tc}(\text{longitudinal}) \times l_{sc}^2(\text{transverse}) \quad (1)$$

The value of l_{tc} can be estimated from knowing the energy width ΔE, and l_{sc} for a simple geometry becomes the product of the de Broglie wavelength (λ_e) and the ratio of the distance (L) to the specimen from the source and the source's width (w), $l_{sc} \approx \lambda_e(L/w)$. For λ_e of 2.5079 pm (200 keV UEM), this gives a coherence volume of about 10^6 nm^3, assuming the simple geometry mentioned. For a real microscope, electron trajectory calculations predict a range of 10^3 to 10^6 nm^3, depending on the number of electrons and the angular spread. The issues of cell volume and brightness of the source are important when considering the prerequisites of high-resolution imaging, through the so-called contrast transfer function, and for the regimes of noninteractive electron statistics. Figure 2 summarizes the key concepts involved in single-electron microscopy, together

with a typical high-resolution image and a temporal profile obtained in UEM.

The Ultrafast Electron Microscope

At the California Institute of Technology (Caltech), three UEM microscopes are in operation; one at a maximum voltage of 120 kV, the second at 200 kV, and the third with high-brightness, pulse-scanning capabilities. Upon the initiation of the structural change of the specimen by heating, or through electronic excitation by the ultrashort clocking pulse, a series of frames for real-space images, and similarly for diffraction patterns or electron energy-loss spectra (EELS), is obtained. In the single-electron mode of operation, which affords studies of reversible processes or repeatable exposures, the train of strobing electron pulses is used to build up the image. By contrast, in the single-pulse mode, each recorded frame is created with only one pulse of 10^5 to 10^6 electrons. By simply flipping two mirrors, one has the freedom to operate the apparatus in either single-electron or single-pulse mode.

The first high-resolution images were obtained in UEM-2 (Fig. 2). Frames of real-space images taken for graphitized carbon display the separations of atomic planes at 3.4 Å. For these carbon-family materials, the temporal response, acquired with EELS, was recorded on the femtosecond time scale, and so were their diffraction patterns in Fourier space (see below). Besides the electron-energy resolution, the apparatus can operate in the scanning transmission (STEM) mode, and with the variants of convergent-beam and near-field UEM imaging, as shown below.

Unlike measurements obtained from the whole of the specimen, microscopy images from a 2000- × 2000-pixel charge-coupled device (CCD) camera provide up to 4 million simultaneous observations, each attributable to a single, independent location on the specimen (subject to point-spread function limitations). As a result, the spatiotemporal changes, frame by frame, can be observed for all specimen points at once, which is the analog of parallel processing, without the spatial averaging. The power of selected-area (pixels) image dynamics was demonstrated in a study of gold following in situ femtosecond heating, at a rate higher than 10^{12} K/s, of the nanometer-thick single crystal (*10*).

Diffraction in Fourier Space: A Prelude

Historically, the discovery of electron diffraction was first made for materials (*14*, *15*) and then, within a few years, for gaseous molecules (*16*). With photoelectric methods, the time resolution in diffraction was advanced, first using 100-ps electron pulses and later with pulses in the 10-ps range; for a review of the early work by Mourou, Elsayed-Ali, and others, see (*17*). With diffraction, the challenge became in clocking structural changes with higher time resolution, and especially in the gas phase for isolated chemical reactions.

At Caltech, by using different generations of instruments (*8*), our research has focused on ultrafast structural dynamics in different phases (*17*, *18*). Experiments have included the following: isolated chemical reactions (*19*, *20*), structural phase transitions (*21*, *22*), molecular interfaces on hydrophobic and hydrophilic substrates (*23*–*25*), and nanowires of optoelectronic materials (*26*). In the groups of Miller, Cao, and Ruan (*27*–*29*), most of the work has been devoted to nonthermal melting and phonon dynamics and to nanoparticles. Typically, in such diffraction studies, the electron pulse contains thousands of electrons, but for subpicosecond electron dynamics (*30*, *31*), 100 or fewer electrons are used and with a novel geometry for the compensation of group-velocity mismatch between light and electron pulses (*22*). Care had to be taken to discern the effect of "surface charging," especially at high fluences (*12*).

Imaging in the Millisecond and Nanosecond Regimes

In conventional microscopes with a field-emission gun (FEG) or cathode heating, processes occurring on seconds or longer time scales are easily accessible. With fast CCD cameras, this scale can reach the millisecond time range. One of the most impressive examples comes from the study of relatively slow catalytic reactions and materials imperfections (*32*). It is difficult in EM to operate the instrument in such a manner as to allow for gas-solid and liquid-solid interactions, because the mean free path of the electrons becomes infinitesimal under these conditions. Gai and Boyes (*32*), in their environmental TEM, achieved atomic spatial resolution in the imaging of nanoparticles participating in catalytic turnover (Fig. 3), and they illustrated how such reactions can be temperature-resolved and time-resolved, at milliseconds and longer times. Similarly, nanoparticles shape change at elevated temperatures, and other phenomena related to materials imperfections can be examined.

With faster detectors, it is possible to reach the submillisecond range, however, not beyond the known response of electronics. Photoelectrons, which were invoked in the diffraction studies discussed above, provide the means to reach much higher time resolution, assuming that the photoelectrons generated by an optical pulse do not suffer from temporal and spatial losses of resolution during the journey to the specimen and on to the detector. Bostanjoglo and co-workers (*33*), in a series of seminal investigations of melting and ablation in thin metal films, obtained nanosecond temporal resolution and micrometer (and later submicrometer) spatial resolution using single pulses. Originally, they detected on a fast oscilloscope the total electron current in the bright field, after the sample had been pumped by a nanosecond laser pulse, obtaining low-resolution patterns. Later, however, with nanosecond electron pulses and deflection plates after the specimen, they obtained with somewhat better spatial resolution two or three images (deflected to different regions of the CCD) for the irreversible process under examination. Hence, the resolution was limited by the nanosecond pulses in the space-charge regime and by the electronics used for the electron beam deflection, which was used to overcome the slow detector response. Figure 3 displays typical frames that were taken with this high-speed recording method (see Fig. 1) in the Berlin laboratory.

In these studies of metal films exposed to high-fluence pulses of 7 to 30 J/cm^2, the focus was on the investigation of surface evaporation, boiling, and gas bubble formation. The images cannot provide structural information because of their low resolution, and for this reason, they invoked diffraction, as in the study of the phase change of crystalline titanium (*34*). Subsequent work at the Lawrence Livermore National Laboratory (LLNL) has further improved the spatial resolution and provided, from a large amount of nanosecond electron diffraction data, the transition time for titanium phase change; the resolution in images can reach tens of nanometers with nanosecond pulses. More recently, the LLNL group extended the high-speed nanosecond recording, in what is referred to as dynamic TEM, into another domain of investigation (*35*), namely the monitoring of reaction fronts in multilayer foils by initiating the reaction (with a light pulse) at one spot on the specimen and observing the front movement with the electron pulse at a distant location (Fig. 3).

These studies are valuable for nanosecond-limited irreversible processes, as discussed below. For them, the spatiotemporal resolution is determined by the fundamental space-charge effect, which was the central issue resolved by single-electron imaging.

4D UEM: Applications and Variants

Breaking the barrier into ultrafast temporal and high spatial resolutions provides the opportunity to explore new applications and to discover new phenomena. A paradigm case of UEM exploration, which illustrates the methodology, is that of the quasi-2D graphite studied in specimens of nanoscale. Graphite is unusual for many reasons, especially for its structure-phase connection to graphene and diamond. For this case, we shall consider below the progression in length and time scales, from those that characterize atomic motions to the macroscopic behavior when emergent function, such as drumming, becomes evident in 4D imaging (Fig. 4).

Prototypical Case: Graphite in 4D Space

Atomic motions. When the layered structure of graphite is subjected to a shock, the structure distorts, and ablation to form graphene (individual sheets of hexagonal sp^2-bonded carbons) may result from its instability. To elucidate the dynamics, a series of images and diffraction patterns were obtained at different times. The Bragg diffraction

shows changes in the position, intensity, and width of the peaks. These changes mirror the dynamics of the atomic positions of the crystal structure, because any increase or decrease in lattice spacings results in changes in diffraction characteristics. The patterns, when analyzed, reveal an initial lattice distortion (in the first 1 to 2 ps) followed by an expansion along the *c* axis of graphite, that is, the axis perpendicular to the carbon-atom planes. The maximum observed expansion of the lattice in 7 ps corresponds to ~1.25% of the *c* axis equilibrium value, 6.7 Å, which is beyond any thermal value, because such a change would correspond to a temperature jump of more than 1500 K. This conclusion is supported by the magnitude of the observed change, which scales correctly with the order of diffraction in both the intensity and the position of Bragg spots (*12*). Theory attributes the formation of graphene from graphite to these compression-expansion dynamics, and they are consistent with recent optical and surface studies of graphite (*12*, *29*, *36*–*38*).

Acoustic resonances and elasticity. On longer time and length scales, following the femtosecond pulse of heating stress, a strain propagates in the nanomaterial, and the strobing electron packets can then be used to probe the elastic modulation that occurs at the speed of sound. In other words, the initial atomic movements transform into acoustic waves of different frequencies and shapes (modes), and, depending on energy, some persist for picoseconds and beyond. This gives rise to an oscillatory (resonance) behavior in both the images obtained in real space and the diffraction patterns recorded in reciprocal space. The coherent resonance has two important features: the frequency and the decay of the amplitude. The latter gives the thickness inhomogeneity of the specimen, which, for the graphite studied, was found to be ±2 nm.

The resonance frequency (Fig. 4) directly relates to the force holding the layers (elasticity) and thickness of the material, in the same way a musical tone will. From these real-time experiments, the stress-strain profile, characterized by Young's modulus, was determined at the nanoscale. These hitherto-unobserved, very-high-frequency resonances (30-GHz range) are unique to the nanoscale dimensions of graphite. The speed of sound in nanographite along the longitudinal (*c* axis) direction is determined to be 4.0×10^5 cm/s, giving Young's modulus of 36.0 GPa. The period observed in the image is the same as that for the diffraction, indicating a direct correlation between the local atomic structure and the macroscopic elastic behavior. Selected-area imaging dynamics played a critical role, because different regions have temporally different amplitudes and phases across the image (*10*, *39*). These observations raise the following question: At what nanoscale would the continuum bulk material model break down?

Membrane mechanical drumming. At even longer time and length scales, new features came into focus in real-space imaging of graphite (*39*). The images displayed the vibrations of mechanical drumming. Upon the impulsive heating at time zero, the image changes considerably with a transition from a chaotic-looking behavior at early times, to quasiperiodicity at intermediate times, and on to a well-defined resonance oscillation emerging at longer times (Fig. 4). In other words, the motion collapses into a final resonance, in this case with a frequency of 1.08 MHz after several microseconds. The behavior is reminiscent of nonlinear couplings between modes of oscillations, but it may also reflect differences in the lifetimes of the modes excited in the nanosites. From this resonance of mechanical drumming of the whole plate, the in-plane (carbon sheets) Young's modulus was obtained, with a value of 0.94 TPa. This value is different by more than an order of magnitude from the *c* axis value, reflecting the strong in-plane chemical bonding and anisotropic behavior.

Chemical bonding and FEELS. In the above applications, the electrons interact elastically with matter, that is, with no loss of their energies. However, it is also possible to record EELS due to inelastic interactions, and when they are femtosecond-resolved (FEELS), we can obtain 3D maps of time-energy-amplitude for the characterization of binding during materials change of valency and phase. In UEM with FEELS, we obtained these 3D plots for graphite, recording frames' changes in 100 fs and for electron energy loss from 0 to 50 eV (Fig. 4). Because in this energy range the electron spectrum displays binding characteristics of the π and σ electrons and of bulk and surface atoms, the change in amplitudes of scattering and energy positions in FEELS is telling of bonding changes with time, following the impulsive energy stress. The dynamics reveal a striking correlation between the compression and expansion of layers on the sub-picometer scale for surface and bulk atoms and the direction of change from sp^2 (2D-graphene) to sp^3 (3D-diamond) electronic hybridization (*11*). Recent scanning tunneling microscopy (STM) investigation (*37*) has revealed domains of these sp^3-type structures in femtosecond (not nanosecond) irradiated graphite, which is consistent with our FEELS observations. A perspective on this 10–orders of magnitude

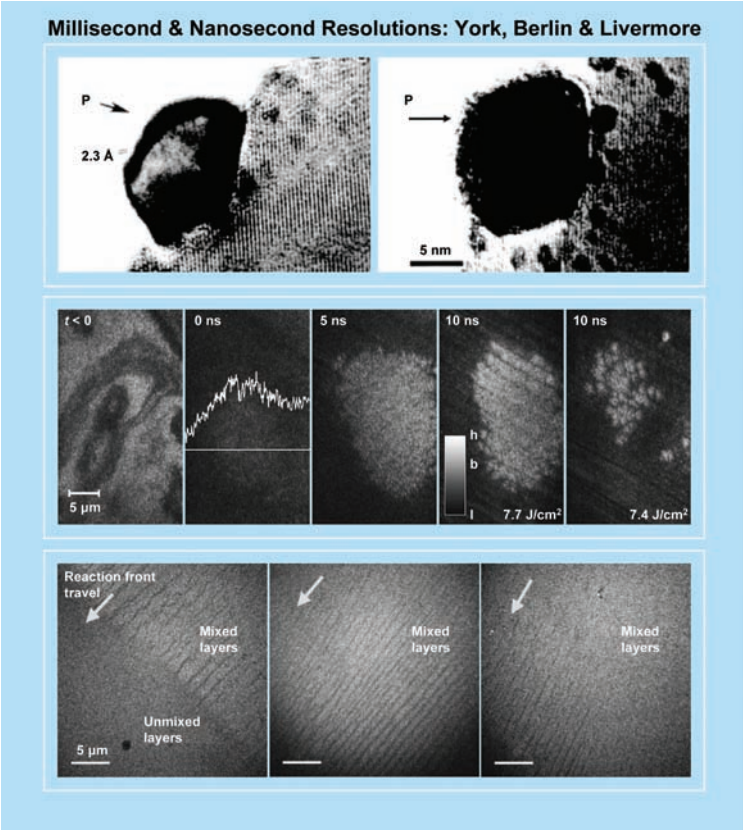

Fig. 3. Millisecond and nanosecond imaging by the groups at York, Berlin, and Livermore. Displayed at the top is the work from the group of Gai (*32*). Shown are in situ atomic-resolution environmental TEM images of Pt/titania catalyst activated in hydrogen at 300°C, with the atomic planes resolved (2.3 Å) in the Pt particle (P). The same particle is shown at 450°C, also in hydrogen, demonstrating the growth of Ti-oxide overlayer and development of Pt clusters. Such an experiment can be ramped at 30 frames per second. The middle panel depicts single shots of explosion in a nickel film acquired with nanosecond resolution. The pattern at time $t = 0$ indicates the intensity change across the line shown with the bar (at $t < 0$) giving the micrometer scale. At $t = 10$ ns, the bar reflects the change in the transmitted intensity of initial liquid (l), bubbles (b), and final hole (h). The fluence is very high (~8 J/cm^2). This panel is adapted from (*55*) of the Berlin group. In the lower panel, shown is the resolution of a reaction front on the microsecond time scale, displaying a transient behavior in the mixed layers. This panel is adapted from the work at LLNL (*35*).

improvement in EELS was recently published by Thomas (*40*).

Functional Nanomechanical Systems: Cantilevers

UEM can also be used to study in situ structural transformations of a material during a function. The change is directly visualized in the variation of the properties of the material itself. As such, the method can be used to optimize and discover new micro- and nanoelectromechanical systems (MEMS and NEMS). Whereas current methods of detection provide insights into the movements of nanoscale structures, direct real-space and -time visualization of modes of oscillations at frequencies pitched in the ultrasonic range (that is, kilohertz to gigahertz) was not possible. Here, we highlight one prototypical study of cantilevers made of nano(micro)crystals of Cu-TCNQ, a quasi-1D semiconductor (*41*).

In UEM, the static structures were determined from a tomographic-like tilt series of images, whereas the in situ temporal evolution was established using the stroboscopic electron packets. A movie of the 3D motions of cantilevers was produced from frames of the optomechanical expansions, which were triggered by the charge transfer from the TCNQ radical anion ($TCNQ^{-}$) to copper (Cu^{+}). The expansions are colossal, reaching the micrometer scale, and the observed resonance oscillations are of two types, longitudinal and transverse, with resonance Q factors that make them persist for up to 1 ms. From them, we obtained Young's elastic modulus (2 GPa), the force (600 μN), and the potential energy (200 pJ) stored. The mechanical function is robust, at least for 100 continuous pulse cycles (~10^{11} oscillations for the recorded frames), with no apparent damage or plasticity. Of the initial optical energy, a minimum of 1% is converted into mechanical motion, but in fact it could reach 10% or more. Nanoscale cantilevers, which were studied similarly, displayed resonance modes of much higher frequencies (*41*).

Irreversible Phase Transitions and Crystallization

For transformations that are irreversible in nature, we explored two types of phase transitions: nucleation and crystallization in silicon and martensitic structural changes in iron. With a single-electron pulse, the process is followed in situ in the microscope, and structural changes are visualized in the images and diffraction patterns. The embryonic stages of crystallization, when observed in real time, elucidate two types of processes involved in the transition from amorphous to crystalline structure in silicon: one that occurs at early times (nanoseconds) and involves a nondiffusive motion, and another one that takes place on a significantly longer time scale (microseconds) (*42*).

The other irreversible phase transition studied with single-pulse imaging is that of the para(ferro)magnetic transformation in iron, from body-centered to face-centered cubic crystal structure. For this transformation, the intermediate(s) involved were arrested in time, and the temporal behavior provides the following time scales for the processes: first, a nanosecond nucleation from incoherent but collective energy-barrier crossing motions of atoms; and second, a barrierless phase growth on the picosecond time scale for nanometer domains (*43*). As mentioned above, such phase changes in titanium (*34*, *44*), silicon (*42*), iron (*43*), and other materials (*12*) can be resolved using single-pulse imaging on the nanosecond and longer time scale.

Variant Techniques: Convergent-Beam, Near-Field, and Tomographic UEM

To study single particles (sites) of nanoscale with UEM, we recently developed 4D nanodiffraction imaging of structural dynamics with convergent electron (pulsed) beams (*45*). Instead of using a parallel electron-beam illumination with a single-electron wave vector, a convergent beam (CB) with a span of incident wave vectors is focused on the specimen. This method of CB-

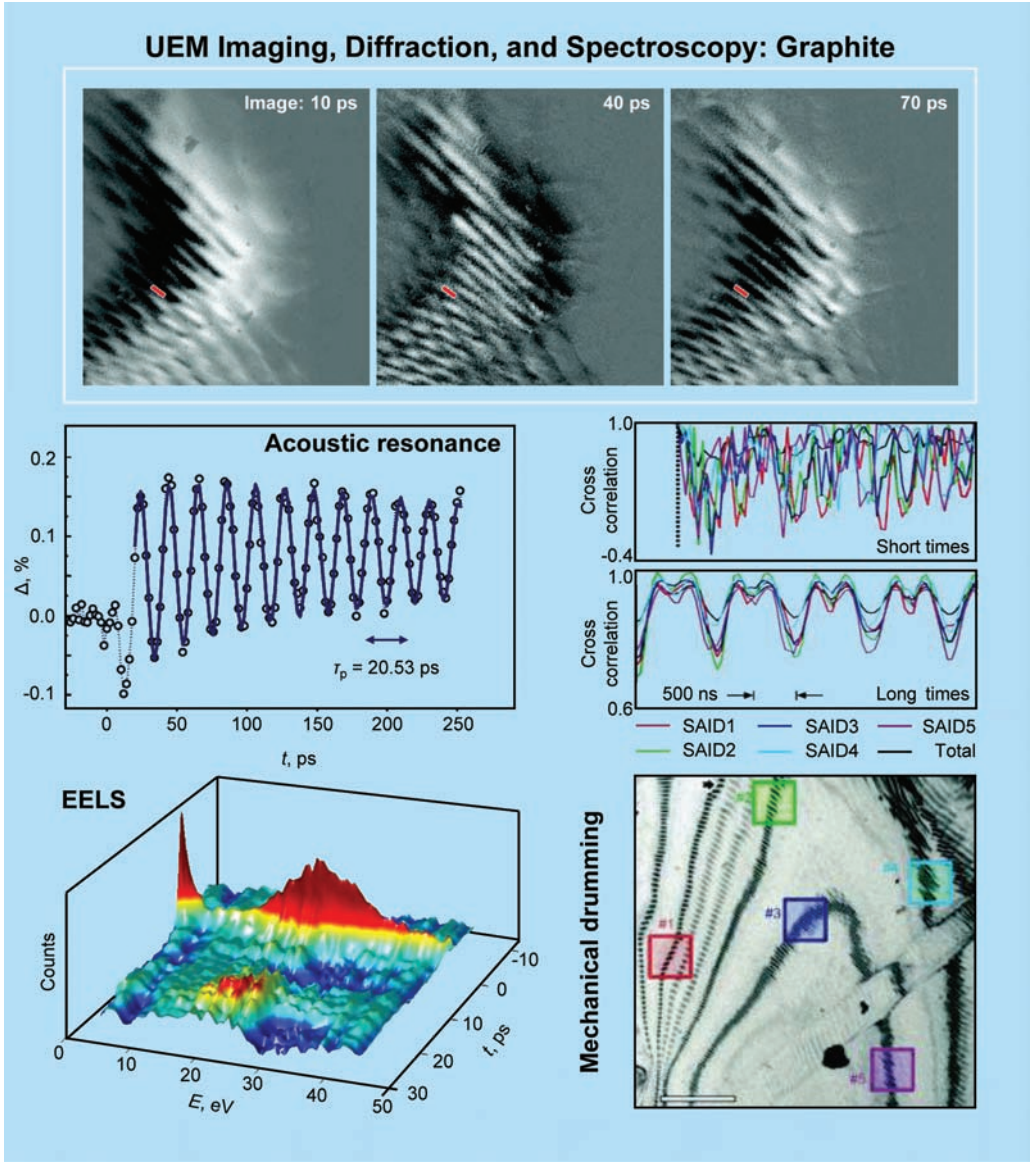

Fig. 4. UEM imaging, diffraction, and spectroscopy of graphite: a prototypical case study. Shown are three frames for the change in the image with time (upper panel), the observed acoustic resonance (center left), the FEELS contour map (lower left), and the drumming resonance observed at longer times (lower right and center right). The selected area image dynamics (SAID) display the observed local resonances. See text and (*10*, *11*, *39*, *56*); the values discussed in the text for resonance frequencies, Young's moduli, and the speed of sound are given in (*56*).

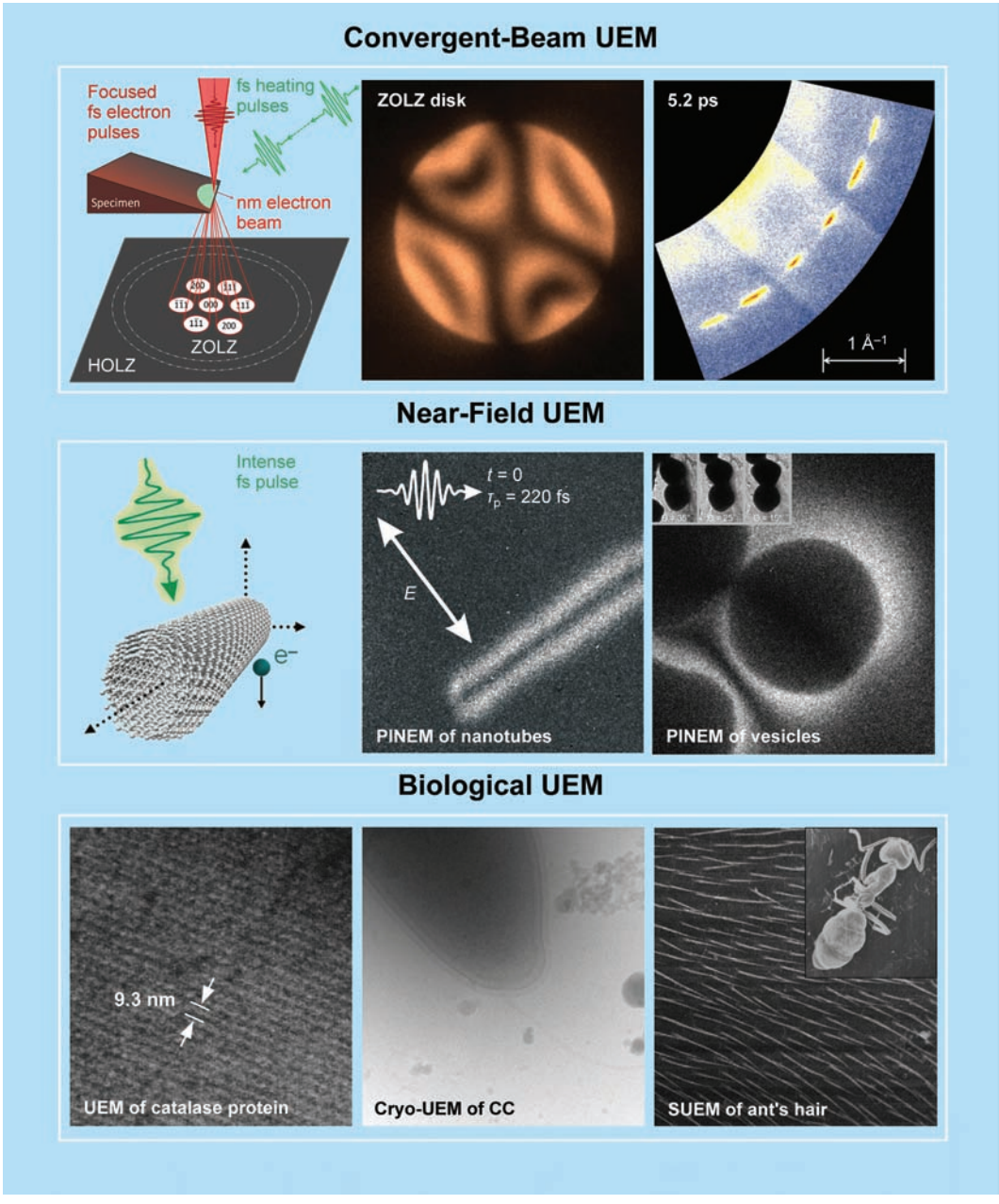

Fig. 5. Convergent-beam, near-field, and biological UEM imaging. The upper panel displays concepts pertinent to CB-UEM together with a typical zero-order Laue zone disk and a nanodiffraction frame taken at 5.2 ps. By following the individual spots in the ring as a function of time, the dynamics of the probed nanoarea of the specimen are obtained [see (*45*)]. Shown in the middle panel is the concept pertinent to PINEM together with the image of a carbon nanotube as obtained using perpendicularly polarized photons. The image was obtained at time $t = 0$ with femtosecond resolution [see (*46*, *47*)]. Also shown (on the right) is the application of PINEM to visualize a protein shell of a liquid-filled vesicle; the inset depicts three tomographic frames showing the spherical shape of the vesicle as seen from different angles. The protein shell "lights up" at $t = 0$ and dims in 200 fs. In the bottom panel, displayed are catalase protein crystal (with the lattice-plane separations of 9.3 nm), bio-UEM micrographs of *Caulobacter crescentus* (CC; the image obtained by cryomicroscopy), and a scanning UEM image of ant's hair. See text.

UEM affords determination of 3D structures with high precision for local areas, reaching below one unit cell. For silicon, the observed structural dynamics (rate of 0.14 ps^{-1}), the temperatures (rate of 10^{14} K/s), and the amplitudes of atomic vibrations (up to 0.084 Å) are all for the local site (10 to 300 nm) probed, not for the bulk material (Fig. 5). We anticipate a broad range of applications of CB-UEM and its variants, especially for structural dynamics of single particles and heterogeneous assemblies.

Another variant UEM technique is 4D tomography, in which the electron pulses, for a given beam focus and at a fixed time delay, give rise to images for a whole series of tilt angles, as recently demonstrated by O.-H. Kwon in this laboratory. When this process is repeated for a sequence of time delays on the femtosecond and nanosecond timescales, a 4D tomograph is constructed. The obtained tomographs constitute a movie that displays the motions of the nanoobject, all visualized at once. This 4D tomography was demonstrated first for carbon nanowire structures, and in Fig. 5, an example is given for a biological structure at three representative angles and at time zero, as obtained by D. Flannigan and B. Barwick of this laboratory.

In general, photons in UEM are used to initiate a change (clocking) for the study of structural or morphological dynamics, but before these structural and morphological changes occur, electronic distributions are altered, with the dynamical changes being on the femtosecond and shorter time scale. It is possible to exploit strong interactions between photons and electrons to open up a new avenue in UEM investigations. Recently, we reported the development of photon-induced near-field EM (PINEM) (*46*) for the probing of interfacial evanescent and ephemeral fields in nanostructures. Only when the field is induced and probed on the ultrashort time scale would it be visualized and controlled for applications in imaging and spectroscopy. In contrast to FEELS, in PINEM we observe gain, instead of loss, of electron energy with, remarkably, 10 or more photons being absorbed by the electron. Such phenomena of energy gain, as electrons and photons team up (*47*), are observed only in the presence of the nanostructure, and they display unique spatial, temporal, and polarization properties of the nanomaterials and biological structures studied (Figs. 2 and 5, and below).

Future Outlook

The tabletop electron microscope is arguably the most powerful scientific instrument because of its three major domains: real-space imaging, Fourier-space diffraction, and energy-space spectroscopy. The scope of applications is wide-ranging, from materials and mineralogy to nanoscience and

biology. Because of the powerful focusing capabilities of electrons, structures can be determined for local (sub)nanosites, and not averaged over micrometers of specimens' dimensions, which, as in x-ray crystallography, would provide higher precision. Whereas optical imaging, which is essential in mapping live cells, locates particles' positions, electron imaging resolves the structures down to the atomic scale.

The integration of the fourth dimension—time—should now transform static imaging into the realm of dynamics in both space and time, and the opportunities are numerous. With environmental high-resolution imaging, it should be possible to study materials and biological systems at controlled conditions, and with circulating fluid cells (*48*), the issue of specimen recovery becomes irrelevant. The advent of near-field and convergent-beam UEM variants opens the door for applications in nanoscale plasmonics and photonics and for studies of heterogeneous processes, such as those involved in the catalytic properties of nanoparticles or in phase transitions. Moreover, the discovery of the photon-induced near-field (PIN) effect, with multiple quanta of energy exchange, may lead into nonlinear electron spectroscopy at the atomic scale, and with recent developments in attosecond optical pulse generation by Krausz, Corkum, and others (*49*), we may soon make possible, with UEM, the imaging of matter's electron dynamics (*50*).

Our first entry into bioimaging resulted in a proof-of-principle UEM visualization of a stained rat cell (amplitude contrast) and, with cryotechniques, the membrane structure of cells in vitreous ice (phase contrast). Proteins were also imaged in real space (Fig. 5). More recently, UEM-3 was developed using a FEG of high brightness and coherence, and with the scanning of the electron probe pulse, we were able to image biological specimens and materials surfaces, as demonstrated by D.-S. Yang and O. Mohammed of this laboratory (see Fig. 5). Using near-field UEM, it was also possible to "light up" the field of a "dark" protein shell forming a liquid-filled vesicle (Fig. 5). The enhanced imaging, by the PIN effect, disappears in a few hundreds of femtoseconds. The potential of recording femtosecond (or longer) time-scale dynamics and arresting specimens' movements, which should result in much sharper images, represent exciting directions of research. Lastly, we have found, based on theoretical studies by M. Lin of this laboratory, that there exist some criteria for taking advantage of the regularity of pulsed dosing, and this concept is now being tested experimentally for the control of energy redistribution and heat dissipation, and hence radiation damage, in bio-UEM.

From a historical perspective, the progress in this field has been made over a century of developments. The discovery of the electron (J. J. Thomson) and its wave character (L. de Broglie) laid the foundation for 2D electron microscopy (M. Knoll and E. Ruska) in the 1930s. Three decades later, 3D image reconstruction from a single projection (D. J. DeRosier, A. Klug, and R. A. Crowther) and from a tilt series (R. G. Hart and others) was achieved, and since then, numerous advances in nanotomography and holography (P. Midgley, D. Muller, C. Colliex, A. Tonomura, and others) have been made [see (*12*)]. The transition to ultrafast electron imaging was accomplished during the past decade, and with the arsenal of variant techniques available, 4D electron microscopy has the potential to decipher the fundamental forces behind the function of complex structures, physical and biological.

References and Notes

1. R. Hooke, *Micrographia* (Royal Society, London, 1665).
2. S. W. Hell, *Science* **316**, 1153 (2007).
3. B. Huang, M. Bates, X. Zhuang, *Annu. Rev. Biochem.* **78**, 993 (2009).
4. W. Min *et al.*, *Nature* **461**, 1105 (2009).
5. M. Knoll, E. Ruska, *Z. Phys.* **78**, 318 (1932).
6. P. W. Hawkes, J. C. H. Spence, Eds., *Science of Microscopy* (Springer, New York, 2007).
7. A. H. Zewail, in *Les Prix Nobel: The Nobel Prizes 1999*, T. Frängsmyr, Ed. (Almqvist & Wiksell, Stockholm, 2000), p. 110.
8. A. H. Zewail, *Annu. Rev. Phys. Chem.* **57**, 65 (2006).
9. A. H. Zewail, V. A. Lobastov, U.S. Patent 7,154,091 (2006).
10. B. Barwick, H. S. Park, O.-H. Kwon, J. S. Baskin, A. H. Zewail, *Science* **322**, 1227 (2008).
11. F. Carbone, O.-H. Kwon, A. H. Zewail, *Science* **325**, 181 (2009).
12. A. H. Zewail, J. M. Thomas, *4D Electron Microscopy: Imaging in Space and Time* (Imperial College Press, London, 2010).
13. T. Folger, *Science* **324**, 1512 (2009).
14. C. Davisson, L. H. Germer, *Phys. Rev.* **30**, 705 (1927).
15. G. P. Thomson, A. Reid, *Nature* **119**, 890 (1927).
16. H. Mark, R. Wierl, *Naturwiss* **18**, 205 (1930).
17. R. Srinivasan, V. A. Lobastov, C.-Y. Ruan, A. H. Zewail, *Helv. Chim. Acta* **86**, 1761 (2003).
18. D. Shorokhov, A. H. Zewail, *J. Am. Chem. Soc.* **131**, 17998 (2009).
19. H. Ihee *et al.*, *Science* **291**, 458 (2001).
20. R. Srinivasan, J. S. Feenstra, S. T. Park, S. Xu, A. H. Zewail, *Science* **307**, 558 (2005).
21. N. Gedik, D.-S. Yang, G. Logvenov, I. Bozovic, A. H. Zewail, *Science* **316**, 425 (2007).
22. P. Baum, D.-S. Yang, A. H. Zewail, *Science* **318**, 788 (2007).
23. C.-Y. Ruan, V. A. Lobastov, F. Vigliotti, S. Chen, A. H. Zewail, *Science* **304**, 80 (2004).
24. D.-S. Yang, A. H. Zewail, *Proc. Natl. Acad. Sci. U.S.A.* **106**, 4122 (2009).
25. S. Chen, M. T. Seidel, A. H. Zewail, *Angew. Chem. Int. Ed.* **45**, 5154 (2006).
26. D.-S. Yang, C. Lao, A. H. Zewail, *Science* **321**, 1660 (2008).
27. B. J. Siwick, J. R. Dwyer, R. E. Jordan, R. J. D. Miller, *Science* **302**, 1382 (2003).
28. H. Park, X. Wang, S. Nie, R. Clinite, J. Cao, *Phys. Rev. B* **72**, 100301 (2005).
29. R. K. Raman *et al.*, *Phys. Rev. Lett.* **101**, 077401 (2008).
30. M. Y. Shchelev, *Quantum Electron.* **37**, 927 (2007).
31. A. Gahlmann, S. T. Park, A. H. Zewail, *Phys. Chem. Chem. Phys.* **10**, 2894 (2008).
32. P. L. Gai, E. D. Boyes, *Electron Microscopy in Heterogeneous Catalysis* (IOP Publishing, Bristol, UK, 2003).
33. O. Bostanjoglo, *Adv. Imaging Electron Phys.* **121**, 1 (2002).
34. H. Kleinschmidt, A. Ziegler, G. H. Campbell, J. D. Colvin, O. Bostanjoglo, *J. Appl. Phys.* **98**, 054313 (2005).
35. J. S. Kim *et al.*, *Science* **321**, 1472 (2008).
36. K. Ishioka *et al.*, *Phys. Rev. B* **77**, 121402 (2008).
37. J. Kanasaki, E. Inami, K. Tanimura, H. Ohnishi, K. Nasu, *Phys. Rev. Lett.* **102**, 087402 (2009).
38. H. Yan *et al.*, *Phys. Rev. B* **80**, 121403 (2009).
39. O.-H. Kwon, B. Barwick, H. S. Park, J. S. Baskin, A. H. Zewail, *Nano Lett.* **8**, 3557 (2008).
40. J. M. Thomas, *Angew. Chem. Int. Ed.* **48**, 8824 (2009).
41. D. J. Flannigan, P. C. Samartzis, A. Yurtsever, A. H. Zewail, *Nano Lett.* **9**, 875 (2009).
42. O.-H. Kwon, B. Barwick, H. S. Park, J. S. Baskin, A. H. Zewail, *Proc. Natl. Acad. Sci. U.S.A.* **105**, 8519 (2008).
43. H. S. Park, O.-H. Kwon, J. S. Baskin, B. Barwick, A. H. Zewail, *Nano Lett.* **9**, 3954 (2009).
44. T. LaGrange, G. H. Campbell, P. E. A. Turchi, W. E. King, *Acta Mater.* **55**, 5211 (2007).
45. A. Yurtsever, A. H. Zewail, *Science* **326**, 708 (2009).
46. B. Barwick, D. J. Flannigan, A. H. Zewail, *Nature* **462**, 902 (2009).
47. F. J. García de Abajo, *Nature* **462**, 861 (2009).
48. N. de Jonge, D. B. Peckys, G. J. Kremers, D. W. Piston, *Proc. Natl. Acad. Sci. U.S.A.* **106**, 2159 (2009).
49. F. Krausz, M. Ivanov, *Rev. Mod. Phys.* **81**, 163 (2009).
50. P. Baum, A. H. Zewail, *Chem. Phys.* **366**, 2 (2009).
51. K. D. M. Harris, J. M. Thomas, *Cryst. Growth Des.* **5**, 2124 (2005).
52. J. M. Thomas, *Angew. Chem. Int. Ed.* **44**, 5563 (2005).
53. J. M. Thomas, *Angew. Chem. Int. Ed.* **43**, 2606 (2004).
54. J. M. Thomas, *Nature* **351**, 694 (1991).
55. H. Dömer, O. Bostanjoglo, *Appl. Surf. Sci.* **208–209**, 442 (2003).
56. H. S. Park, J. S. Baskin, B. Barwick, O.-H. Kwon, A. H. Zewail, *Ultramicroscopy* **110**, 7 (2009).

57. In the course of developments at the Center for Ultrafast Science and Technology (UST), I have enjoyed the scholarly discussions with and enthusiasm of J. M. Thomas of Cambridge University, the fruit of which resulted in his overview articles (*40*, *51–54*) and our joint monograph (*12*) on 4D EM. The dedication and hard work of members of the UST Center made possible the story told here. I particularly wish to acknowledge the effort of D. Shorokhov in helpful discussion and in manuscript preparation. This research was carried out with support from NSF and the Air Force Office of Scientific Research in the Physical Biology Center for UST supported at Caltech by the Gordon and Betty Moore Foundation.

10.1126/science.1166135